ELSEVIER

Journal of Nuclear Materials 281 (2000) 22–33

journal of nuclear materials

www.elsevier.nl/locate/jnucmat

Beta radiation effects in ^{137}Cs-substituted pollucite

N.J. Hess [a,*], F.J. Espinosa [b], S.D. Conradson [b], W.J. Weber [a]

[a] *Pacific Northwest National Laboratory, P.O. Box 999, Richland, WA 99352, USA*
[b] *Los Alamos National Laboratory, P.O. Box 1663, Los Alamos, NM 87545, USA*

Received 17 February 2000; accepted 31 May 2000

Abstract

The effect of high-energy beta radiation on the long-range and local structure of ^{137}Cs-substituted $CsAlSi_2O_6$ (pollucite) was studied by X-ray diffraction (XRD) and X-ray absorption spectroscopy (XAS) techniques at the Cs K-edge. Analysis of the XRD pattern of pollucite with an absorbed dose of 10^{18} beta decays/g using Rietveld analysis indicates a 0.5–1% volume expansion of the tetrahedral structure as measured at 50 K and a minor displacement of the Cs cation toward the face of one of the six-membered rings. Analysis of the real-space pair-distribution function obtained from Fourier transformation of the diffraction pattern indicates significant correlated movement of the (Si,Al)–O pairs and large static disorder between Cs–O pairs. Analysis of the Cs K-edge XAS revealed substantial contributions from the Cs atomic X-ray absorption. This likely results from the exceedingly long Cs–O bond distances in the pollucite structure, which diminish the fine structure of the XAS oscillations, and the destructive interference of the backscattered photoelectron from static disorder between Cs–O pairs. In addition, a significant lengthening of the Cs–Cs interatomic distance was observed.

PACS: 61.10.–i; 61.10.Ht; 61.10.Nz

1. Introduction

Reprocessing of spent nuclear fuel has resulted in the generation of enormous quantities of high-level radioactive liquid waste containing ^{137}Cs and other decay products. Although, separation of ^{137}Cs and other heat-generating isotopes facilitates treatment of the liquid wastes, specialized waste forms are then needed for long-term storage of ^{137}Cs-rich wastes. Potential waste forms for ^{137}Cs storage include borosilicate glass, glass–ceramics, cesium-loaded zeolites, and pollucite. Of these candidates, pollucite, $CsAlSi_2O_6$, offers the following advantages. The pollucite structure can accommodate more than 40 wt% Cs into its structure and, as a result, will produce a highly dense waste form. As a pollucite waste form is denser than the glass–ceramic or zeolite-based alternatives, significant cost-savings result due to the smaller volume of material to be stored. In addition, the measured and calculated solubility of pollucite, as well as the leachability and mobility of Cs in the pollucite structure are approximately three orders of magnitude less than that measured for silicate glass [1]. Due to these advantages, researchers at PNNL [2,3] are also examining the use of Ti-substituted pollucite, $CsTiSi_2O_{6.5}$, as a waste form for TiO_2-rich wastes that have very low solubility in borosilicate glass. The effect of ^{137}Cs decay, involving the emission of beta-particles and transmutation of Cs to Ba, on the integrity of the waste form is a concern relevant to all potential ^{137}Cs long-term waste forms. In addition to the emission of 0.5 MeV beta-particles, the decay of ^{137}Cs generates 0.6 MeV gamma radiation, which presents a significant health hazard and contributes to the absorbed dose of the waste forms in a repository or during interim storage. In the present study, gamma radiation does not contribute much to the absorbed dose of the sample. Due to the small size of the original sample (a disk 4 mm in diameter and 1.5 mm thick), nearly all the self-emitted gamma radiation escapes the sample without much interaction (i.e., gamma self-absorption is negligible). Under repository or interim storage conditions for

* Corresponding author. Tel.: +1-509 376 9808; fax: +1-509 372 1632.
E-mail address: nancy.hess@pnl.gov (N.J. Hess).

0022-3115/00/$ - see front matter
PII: S0022-3115(00)00191-4

actual waste forms, there will be a significant background of gamma radiation from the array of waste canisters that will contribute significantly to the total absorbed dose.

Most research on radiation effects in waste forms has focused on alpha decay, and the associated recoil nuclei of the actinide elements, that produce several orders of magnitude more displacements per decay than beta decay [5,6]. These atomic displacements result in the formation of defects, such as lattice-site vacancies and interstitial ions, and in many cases, the accumulation of such radiation-induced defects can eventually render a crystalline material amorphous (i.e., lacking long-range order). The Ba-recoil nuclei generated by ^{137}Cs decay has an energy of only 8 eV. In typical crystalline oxide materials, the energy required to displace an atom from its atomic position is about 20–60 eV [6]; thus, Ba displacement is highly unlikely and ballistic collisions involving the Ba-recoil nuclei will result in negligible atomic displacements. However, the energy barrier to Cs self-diffusion in pollucite along the $[\bar{1}\,2\,\bar{2}]$ direction to the vacancy at the center of the six-membered aluminosilicate ring has been calculated to be only 6.8 eV [1]. Thus, a beta-recoil nucleus with the appropriate trajectory could result in the displacement of a Ba ion, assuming that there is no effect of the reduced radii and valence change on the magnitude of the energy barrier created. If only ionic size is taken into consideration, the energy barrier for diffusion is expected to be lower [1]. The additional charge on the Ba^{2+} ion may have little effect on the energy barrier because the overlap of the electron density of the Ba^{2+} with the oxygen atoms of the six-membered ring is expected to be minimal [1]. Ionization may also impact diffusion through the creation of trapped electronic excitations resulting in structural defects that can increase or lower the energy barrier to diffusion.

The beta-particles themselves can also impart energy to the constituent atoms through ballistic collisions. However, due to the small electron mass, this energy is typically quite small. The maximum energy transferred, E_d, to an ion from a collision with a beta-particle can be calculated from Eq. (1) [6]:

$$E_d = 2E_e(E_e + 2m_e c^2)/Mc^2, \quad (1)$$

where E_e is the energy of the beta-particle, m_e the electron rest mass, c the speed of light, and M is the mass of the ion hit by the beta-particle [6]. The maximum energy transferable to O, Al, Si, and Cs atoms by this process is 106, 63, 61, and 12 eV, respectively; however, the probability for maximum energy transfer is low. In addition to the primary beta-particle collisions, secondary collisions, especially those involving the lighter O, Al, or Si atoms, can result in the transfer of energy that may cause subsequent atomic displacements. While the maximum energy transferable among O, Al, and Si atoms in idealized secondary collisions is high, >92% of the incident energy, the maximum energy transferred from these light ions to Cs is lower, 38–57%. Thus, the maximum energy transferable to Cs through secondary collisions is on the order of 35–40 eV. However, the probability of successive maximum energy transfers is small. Since typical displacement energies are on the order of 20–60 eV [6], one would expect, on an average, about one displacement per beta-decay event, with most of the displacements involving oxygen atoms and to lesser extent Al and Si atoms.

The stability of defects created by collisions with beta-recoil nuclei and beta-particles is largely dependent on the thermal energy available to allow the displaced atoms (i.e., interstitials) and vacancies to either migrate or recombine. One source of thermal energy is the absorption of the beta-particle energy, which results in self-heating. The amount of self-heating depends on the activity of the sample, the thermal conductivity of the material, the mean free path of beta-particle and the geometry of the sample. As an upper estimate, we assume that all emitted beta-particles are absorbed by the sample. The thermal conductivity of pollucite is not known; however, the thermal conductivity of a zeolite with similar composition, Na–A, $NaAlSiO_4$, has been estimated at 0.6 W/m K [7]. The amount of self-heating is estimated to be negligible, less than 5 K, due to the low activity of the sample and the small sample size.

The majority of the energy of beta-particles is dissipated by ionization processes that have a significant impact on materials in which solid-state radiolytic damage is likely. An important aspect of beta-decay in nuclear waste forms, compared to alpha-decay, is that it occurs over relatively shorter time scales (several hundred years), and any radiation effects that may occur are a near-term concern for health and safety. An additional aspect of beta-decay associated with the fission products is the transmutation of isotopes in the decay process. The resulting changes in chemistry, valence, and ionic radius may not be readily accommodated in the waste form. For example, pollucite synthesized from oxides can accommodate more than 40 wt% Cs with an ionic radius of 0.188 nm, but only 10 wt% Ba with an ionic radius of 0.160 nm upon which a second phase $BaAl_2O_4$ is formed [4]. Ba^{2+} in 12-fold coordination has an ionic radii equivalent to that of K^+, for which there is an end member analog to pollucite, leucite ($KAlSi_2O_6$). Therefore, the limited solubility of Ba in pollucite most likely results from ineffective charge compensation mechanisms to accommodate divalent Ba in the pollucite structure. However, we note that the process by which the transmutation product Ba accumulates (i.e., spontaneous transmutation) will differ significantly from synthesis from oxides. Since phase separation is a kinetically limited process, the response of the pollucite structure might result in either enhanced or reduced solubility of Ba.

The goal of these investigations is to characterize the defects created by transmutation and beta-radiation processes. We group these processes into ballistic processes, resulting from collisions of atoms with the Ba-recoil nuclei and the 0.5 MeV beta-particles, ionization processes that are largely limited to the aluminosilicate framework, and chemical processes resulting from the transmutation of Cs^+ to Ba^{2+} with the corresponding ionic radii and valence changes. The sample selected for evaluation has accumulated approximately 10^{18} beta-decays/g, which is equivalent to an absorbed dose of 6.3×10^7 Gy and approximately 5×10^{-5} displacements per atom (dpa). Note that the calculated absorbed dose is based only on the dose from the beta-particles because of the limited self-absorption of gamma radiation. In 1984, the amount of ^{137}Cs substituted in the pollucite was 0.035 mole fraction, with the remainder being ^{133}Cs. Based on a 30.04 year half-life, the amount of Ba now incorporated in the structure is 0.012 mole fraction. A suite of spectroscopic tools has been utilized to characterize the radiation effects on a range of length scales. These include the X-ray diffraction (XRD) [8], the real space analysis of the diffraction pattern or pair distribution function analysis (PDF) [9], and extended X-ray absorption fine structure spectroscopy (EXAFS) [10]. The combination of these techniques provides structural information at the atomic to next nearest neighbor length scale (EXAFS), from nearest neighbor to ~1.0 nm length scale (PDF), and at the bulk length scale (XRD-Rietveld analysis).

Pollucite belongs to a family of aluminosilicates that includes leucite ($KAlSi_2O_6$) and analcite ($NaAlSi_2O_6 \cdot H_2O$). These aluminosilicates are based on an (Si,Al)–O tetrahedral framework in which the tetrahedra are linked by sharing corners to form four-, six-, and eight-membered rings. A feature unique to this family is the formation of elongated cages, the ends of which are bound by six-membered rings and the sides of which are composed of three elongated eight-membered rings. These cages accommodate large cations such as Cs^+ and Rb^+ (Fig. 1(a)). Cationic migration through these cages requires that the cation to pass through the face of the six-membered rings. The diffusion of Cs^+ in pollucite is effectively hindered by the energy barrier presented by the six-membered ring, even at 1000 K, but the smaller Na^+ ion is quite labile at room temperature [1]. In addition, this family shows similar transformation behavior between high temperature cubic structures and low temperature tetragonal structures. The transition temperature decreases with increasing cationic radii. At temperatures greater than 373 K the pollucite is cubic with $a = 1.36693$ nm, and upon cooling it gradually becomes tetragonal with $a = 1.36524$ nm and $c = 1.37216$ nm at room temperature [11]. In cubic pollucite, the eight-, six- and four-membered rings are normal to the two-, three-, and four-fold symmetry axes, respectively. In tetrahedral pollucite, the eight-member rings become further elongated commensurate with increased puckering of the two four-membered rings at each end (Fig. 1(b)). Adjacent Cs cations are separated from each other by 0.48 and 0.58 nm measured normal to the eight- and six-membered ring faces, respectively. The Cs cations sit slightly offset from the center of the cage with the average Cs–O distance of 0.36 nm for oxygen atoms belonging to the eight-membered rings. In contrast, the average Cs–O distance for oxygen atoms belonging to the six-membered rings is 0.39 nm.

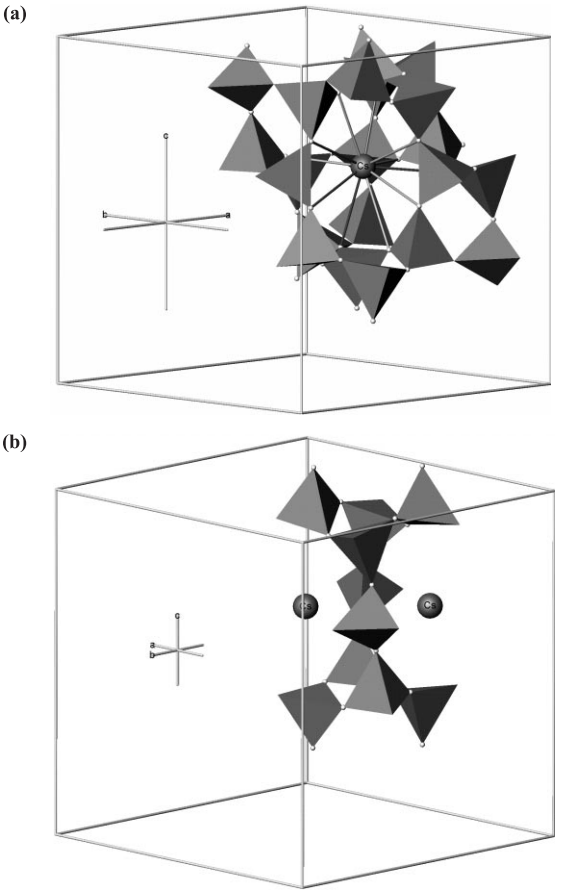

Fig. 1. (a) View of the Cs cage formed by three eight-membered and two six-membered rings. (b) View of along [1 1 0] showing the Cs–Cs separation by an eight-membered ring.

2. Experimental

Stoichiometric ^{137}Cs-doped pollucite was obtained from ORIS-CIS Bio International, France as a sealed beta source, originally used for tumor implant treatments. The ^{137}Cs-substituted pollucite was synthesized by mixing colloidal silica solution with solutions of

aluminum and cesium nitrates in stoichiometric proportions. The solution was evaporated while stirring, followed by calcination at 793–813 K until decomposition of the cesium nitrate occurred. The resulting amorphous calcined material was ground in ether to 10 μm particle diameter. In an atmosphere of 100% humidity at 373 K, the ground powder behaved plastically and was formed into pellets by simple compaction at 250 Pa. The pellets were then sintered in two stages; at 1243 K for 2 h followed by 5 h at 1473 K. The density of the resulting material was on the order of 3.3 g/cm^3, which is in good agreement with the calculated theoretical density of 3.244 g/cm^3. For these studies, approximately 30 mg of the pollucite pellet was removed from the stainless steel encapsulation and mixed with collodion amyl-acetate solution. The resulting slurry was then loaded into a sample holder and triply contained with Kapton, a radiation-resistant mylar.

The XRD data were acquired at the Stanford Synchrotron Radiation Laboratory (SSRL) beamline 7-2. A Si standard (NIST 640b) was used for calibration purposes. The sample was mounted in a He flow cryostat, and the temperature was adjusted to 50 K. The data were collected in symmetric transmission geometry. For Rietveld analysis, the incident X-ray energy was tuned at 22.163 keV (Ag Kα_1 emission line energy), while for real space PDF analysis it was tuned at 31 keV. A Ge solid-state detector coupled to a digital amplifier was used to measure the scattered intensity. Appropriate energy windows were set up to measure the coherent and incoherent (Compton scattering) intensities. The intensity of the incident beam was monitored with an ionization chamber. The data were normalized for flux and corrected for experimental effects, such as detector dead time and absorption. For Rietveld analysis, the data were acquired in two-theta steps of 0.02° up to 50° in two-theta. For PDF analysis, data were acquired in steps of 0.01 Q where $Q = 4\pi\sin(\theta)/\lambda$. It was not possible to acquire data to a maximum Q of $\sim$2.6 nm^{-1} because the signal-to-noise ratio became unfavorable beyond $Q = 1.2$ nm^{-1}. This is typical for amorphous compounds where high Q data are strongly diminished or for crystalline compounds with large disorder. Since our measurements were performed at 50 K, static disorder rather than thermal is likely to cause the lack of signal at high Q. XRD data were analyzed using the Rietveld refinement software GSAS [12]. The data for PDF analysis were further corrected for background scattering from the containment and Compton scattering [13]. Further data reduction to obtain the total structure factor $S(Q)$ was obtained following standard procedures [14]. The reduced atomic distribution function, $G(r)$ was finally obtained from the sine Fourier transform of the interference function $Q[S(Q)-1]$. Low frequency residuals due to errors in normalization of the interference function were corrected by back-transforming the low-r region (<0.12 nm) of $G(r)$ and subtracting it from the interference function [15]. The reduced atomic distribution function $G(r)$ was analyzed using the program PWID [16] in which multiple gaussians were associated with atomic pairs in the structure. The position, width and amplitude of the gaussians were set as refinable parameters. The reduced structure factor $G(r)$ was then calculated. Finally, the calculated $G(r)$ was convoluted with the function $S(r) = \sin(Q_{\max}r)/r$ to account for termination ripples created by the limited Q range of the data [16].

X-ray absorption experiments were conducted at the wiggler end-station 4-2 of the SSRL. A monochromator with silicon [2 2 0] crystals was used to access the high-energy Cs K-edge at 36.005 keV. Ba K-edge XAS was attempted, but the Ba content in this sample was below the detection limit for XAS measurements and no absorption edge was observed. The X-ray absorption spectra were collected at liquid nitrogen temperature in both the transmission mode, using ionization chambers filled with argon gas, and fluorescence mode, using a 13-element Ge detector. Energy calibration for the Cs K-edge was performed by assigning the first inflection point in the absorption edge of a CsCl standard to 36.005 keV (the ionization energy of the 1s atomic level of Cs). The data were acquired to photoelectron wavenumber $k = 1.4$ nm^{-1}, where $k = [(2m/\hbar^2)(E - E_0)]^{1/2}$, E is the incident X-ray energy and E_0 is 36.005 keV. The signal-to-noise ratio of the absorption spectra collected in the transmission mode was higher than that collected in the fluorescence mode. Therefore, subsequent data analysis was only performed on the absorption spectra collected in the transmission mode. The absorption spectrum was normalized by fitting a second-order polynomial through the pre-edge region and a third-order polynomial through the post-edge regions setting the difference at E_0 to unity. The EXAFS oscillations were extracted by fitting a polynomial spline function through the post-edge region. The number and position of the nodes in the spline were varied to minimize the integrated intensity in the Fourier transform moduli (FTM) of the EXAFS between 0 and 0.2 nm. EXAFS nodes are selected as end points for a Fourier transform region and a sine window function is used to reduce the magnitude of termination ripples. Note that all FTM have not been corrected for the photoelectron phase shift and as a result the peaks appear to be 0.02–0.05 nm shorter than the actual distance.

3. Results

3.1. X-ray diffraction

The observed diffraction lines were indexed in terms of a tetragonal structure and are close to those reported

Table 1
Coordinates and isotropic displacement parameters for ^{137}Cs doped pollucite at 50 K[a]

Atom	X	Y	z	U_{iso}	
Cs	0.3647	0.3629	0.13490	0.0404	
T1	0.0773	0.3805	0.16569	0.0381	
T2	0.1626	0.5960	0.12363	0.0350	
T3	0.3851	0.6550	0.08457	0.0236	
O1	0.1306	0.2915	0.10220	0.0362	
O2	0.1236	0.4813	0.12304	0.0362	
O3	0.1178	0.6535	0.22059	0.0362	
O4	0.1198	0.6575	0.03151	0.0362	
O5	0.2840	0.5933	0.12431	0.0362	
O6	0.4764	0.6160	0.15400	0.0424	
Interatomic distances (nm)					
Cs–O1	0.33705	T1–O1	0.16554	Cs–Cs	0.48812
Cs–O1	0.32721	T1–O1	0.16392	Cs–Cs	0.48084
Cs–O2	0.36687	T1–O2	0.16245	Cs–Cs	0.54224
Cs–O2	0.35440	T1–O4	0.16198		
Cs–O2	0.37067	T2–O3	0.16686		
Cs–O3	0.34834	T2–O4	0.16319		
Cs–O3	0.35080	T2–O5	0.16576		
Cs–O4	0.33171	T2–O2	0.16526		
Cs–O4	0.34281	T3–O3	0.16247		
Cs–O5	0.33342	T3–O5	0.17062		
Cs–O5	0.38757	T3–O6	0.16595		
Cs–O6	0.37840	T3–O6	0.16466		
Cs–O6	0.34144				
Interatomic angles (deg)					
O1–T1–O1	110.6	O2–T2–O3	109.3	O3–T3–O5	110.0
O1–T1–O2	104.9	O2–T2–O4	111.6	O3–T3–O6	112.5
O1–T1–O4	113.5	O2–T2–O5	107.5	O3–T3–O6	107.8
O1–T1–O2	109.2	O3–T2–O4	104.7	O5–T3–O6	105.2
O1–T1–O4	106.0	O3–T2–O5	111.9	O5–T3–O6	109.0
O2–T1–O4	112.7	O4–T2–O5	111.9	O6–T3–O6	112.2

[a] Space group: I $4_1/a$; $a = b = 1.364390(33)$, $c = 1.38145(6)$ nm; density: 3.235 gm/cm^3. $\sigma_{max}(xyz) = 0.0008$; $\sigma_{max}(U_{iso}) = 0.02$; $\chi^2 = 1.375$.

for tetragonal pollucite by Palmer et al. [11]. No attempt was made to differentiate between tetrahedral Al and Si atoms. In the following discussion, the symbol T will be used to represent Al or Si atoms. Fractional coordinates and thermal factors of the Cs and T atoms were refined readily; however, the refinement of the oxygen fractional coordinates and thermal factors presented a greater difficulty. An iterative procedure was adopted in which only selected oxygen parameters were varied at a time. Although this procedure led to convergence, unreasonable T–O bond lengths and O–T–O angles resulted. Therefore, the values for T–O bond lengths and O–T–O angles were constrained to a range appropriate for TO_4 tetrahedra. The results of the refinement using this approach are listed in Table 1 and a comparison of the experimental and calculated XRD patterns is shown in Fig. 2. The sample was found to be tetragonal with space group I $4_1/a$ and lattice parameters $a = b = 1.364390(33)$ nm and $c = 1.38145(6)$ nm. The space

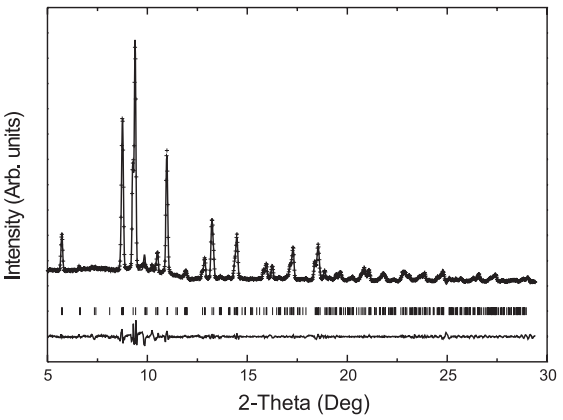

Fig. 2. Observed (crosses) and calculated (line) XRD profiles. Below, the short vertical bars mark the positions of bragg reflections. The difference between the observed and calculated diffraction profiles is shown in the lower part of the figure.

group is the same as determined by Palmer et al. [11]; however, the lattice parameters are approximately 1.0% and 0.4% larger, respectively, than Palmer's lattice parameters interpolated to 50 K [11]. The lattice parameters are also in close agreement to those of Yanase et al. [17] extrapolated to 50 K; however, their structure was refined to a different space group, I $4_1/acd$, which is inconsistent with our diffraction results. While the fractional coordinates are nearly identical to those observed by Palmer et al. [11], the thermal parameters are significantly larger suggesting greater disorder in our sample. Large thermal parameters have been observed in other pollucite samples [2,11,17]. Typically, larger than expected lattice parameters can be explained by the substitution of cations with larger ionic radii into the lattice or structural disorder. Substitution-induced lattice expansion is unlikely for this pollucite sample since X-ray fluorescence analysis indicates the absence of elemental impurities. Structural disorder leading to lattice expansion could be due to synthesis conditions, transmutation effects [18], radiation-induced defects, or lattice distortions due to trapped electronic excitations. However, the pollucite was fully dense when produced, so it is unlikely that the synthesis conditions resulted in expanded lattice parameters. The effect of transmutation processes is expected to be minimal because the initial mole fraction of ^{137}Cs in this sample is low. In fact, due to the smaller ionic radius of Ba^{2+}, the transmutation of Cs to Ba would actually result in a reduction of lattice parameters, if the change in valance is ignored. However, the effect of valence change and defects created by associated ballistic collisions are difficult to evaluate; therefore, the expanded lattice may reflect swelling due to the accumulated radiation and transmutation-induced defects.

3.2. Pair distribution function

The results of the fit to the PDF are summarized in Table 2 and a plot of the calculated and experimental $G(r)$ is shown in Fig. 3(a). The contribution of each atomic pair to the total atomic distribution function was identified using the results of the Rietveld refinement of the diffraction data as input parameters to the program

Table 2
Results of the multiple gaussian fit of the atomic pair distribution function

Pair	Position (nm)	Sigma
T–O	0.17 (1)	0.02 (1)
O–O	0.25 (1)	0.02 (1)
T–T, Cs–O	0.34 (1)	0.17 (1)
Cs–T	0.41 (1)	0.31 (4)
Cs–Cs	0.49 (1)	0.12 (2)
Cs–Cs	0.57 (1)	0.12 (2)

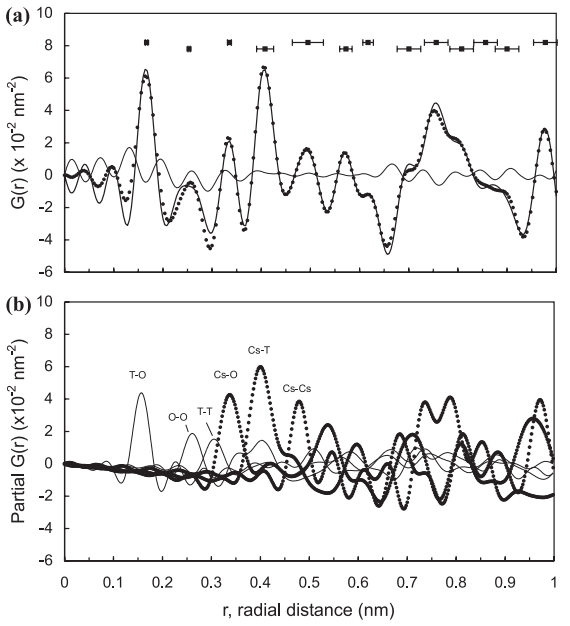

Fig. 3. Comparison of the experimental PDF with modeled PDF: (a) experimental PDF (circles), model PDF using gaussians (thick solid line) and the difference curve (thin solid line). Positions of the gaussians are on top of peaks with their corresponding sigmas; (b) the calculated partial reduced pair distribution function. The contributions from each pair are labeled on top of peaks. Pairs involving Cs are shown with thick dashed lines. Note that these pairs dominate the PDF at radial distances greater than 0.3 nm.

PDFFIT [19]. From this simulation, we discovered that decreasing the Debye–Waller factors from the values obtained in the Rietveld refinement gave a better agreement with the PDF experimental data. On the basis of this observation, we conclude that the large thermal factors obtained in the Rietveld refinement were due to static, long-range disorder. The partial contributions from the different atom pairs were calculated and are shown in Fig. 3(b). This allows assignment of each gaussian of the PWID fit to an atomic pair.

The first gaussian peak at 0.17 nm corresponds to the T–O pair originating from the T–O bond of the TO_4 tetrahedral unit (see Fig. 3). The second gaussian peak at 0.25 nm represents an O–O pair and reflects the O–O separation along the edges of the TO_4 tetrahedral unit. From analysis of the diffraction data, the average O–O separation is 0.267 nm. The disparity between the PDF and the diffraction determination is most likely because of the Fourier ripple, which results from the limited Q range of the data that distorts the position of the O–O pair. The magnitude of the Fourier ripple is clearly observed in Fig. 3(a) by the oscillations at distances less than 0.17 nm. The third gaussian peak at 0.34 nm has two components assigned to T–T and Cs–O pairs. The

T–T pair contribution, which reflects the distance between coordinating tetrahedral atoms of corner-sharing tetrahedra, has a maximum distribution based on the diffraction result at 0.315 nm that is shorter than the 0.34 nm determined from the gaussian fit. Similarly, the Cs–O pair contribution, which represents the 13 oxygen nearest neighbors to Cs, have a bimodal maximal distribution at 0.335 and 0.388 nm based on the diffraction result. The appearance of the third gaussian peak at an intermediate position between the T–T and Cs–O pairs likely indicates that the resolution of the PDF experiment is not sufficient to resolve the two contributions, and the observed peak occurs at an intermediate value. The fourth gaussian peak at 0.41 nm is dominated by Cs–T pair contributions with minor T–O pair contributions. The Cs–T pairs represent the six- and eight-membered rings of the aluminosilicate framework that forms the channels in which the Cs atoms reside. For this gaussian peak, there is an excellent agreement with the diffraction result, the experimental PDF and the calculated PDF. The fifth gaussian peak at 0.49 nm is the most distant peak for which the contributions can be readily identified. It arises from Cs–Cs pairs that represent the adjacent Cs atoms separated by the face of the eight-membered rings and some minor Cs–T pair contributions. The Cs–Cs distance of 0.49 nm is in good agreement with the distance of 0.485 nm determined from the diffraction data. The sixth peak at 0.57 nm has contributions from Cs–Cs, Cs–T, and T–T pairs. The distance of this peak does correspond to the Cs–Cs interatomic distance between Cs atoms separated by the face of the six-membered rings determined by the XRD data, although because of the multiple contributions to this peak the correspondence may be fortuitous.

3.3. X-ray absorption

The background-subtracted, normalized Cs K-edge absorption spectra of pollucite is shown in Fig. 4(a). As a result of the long core-hole lifetime at this energy, the absorption edge spans approximately 30 eV, and the XANES profile is relatively featureless. Also apparent in the inset of Fig. 4(a) is the low amplitude of the EXAFS oscillations. Qualitative results are best described in the Fourier transform moduli (FTM) of the reduced EXAFS. A Fourier transform was taken over the EXAFS region $0.265 < k < 1.25$ nm^{-1}. The FTM in Fig. 4(b) reveals a large amplitude peak centered at approximately 0.20 nm. As there are no expected Cs neighbors in the structure at distances between 0.22 and 0.25 nm, we assume that this feature has no structural origin and that must be due to insufficient background subtraction (for EXAFS analysis purposes). Features at low-r in the FTM are interesting by themselves since they could contain information about the chemical environment of the absorbing atom or from the absorbing atom itself.

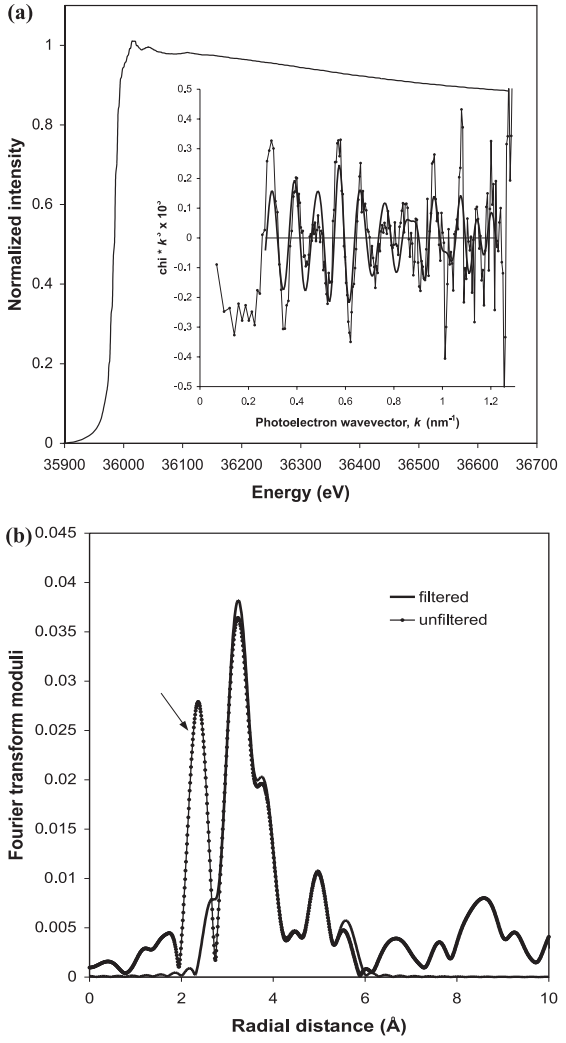

Fig. 4. (a) Normalized X-ray absorption spectrum and EXAFS (inset) before (thin line) and after filtering (thick line). (b) Fourier transform moduli of the unfiltered (thin line) and filtered (thick line) EXAFS. Atomic EXAFS or multielectron processes produce the low R feature, indicated with an arrow, that is not fully removed in the spline subtraction but is removed by filtering.

To clarify this point, we note that the EXAFS oscillations are defined by $\chi(k) = [\mu(k) - \mu_0(k)]/\mu_0(k)$, where k is the photoelectron wavenumber, $\mu(k)$ is the X-ray absorption coefficient and $\mu_0(k)$ is the atomic X-ray absorption coefficient. In a conventional EXAFS analysis, $\mu_0(k)$ is assumed to be smooth and is usually replaced by a spline function, as we described in Section 2. However, $\mu_0(k)$ is not necessarily smooth. It has been shown that the atomic background is expected to contain features associated with the many-body relaxation of the atomic charge that could produce low-r peaks in the FTM [20]. An alternative explanation for low-r peaks has been

given by the photoelectron backscattering in the periphery of the absorbing atom [21]. This phenomenon, called "atomic" EXAFS (AXAFS) reflects the embedded nature of the absorbing atom in the potential of the crystal and could contain information about the chemical bond and interstitial charge distribution [22]. It has been claimed to be the cause of low-r features in the FTM of several systems [23–25]. Further investigation is under way to clarify the nature of the low-r peak in the FTM (Fig. 4(b)). To remove this low frequency contribution, the EXAFS were filtered by taking a back Fourier transform over the range from 0.22 to 0.60 nm. A comparison of the filtered and unfiltered EXAFS and Transform in Fig. 4(b) reveals that the significant features are retained.

The filtered EXAFS was fit over the photoelectron wavevector range from 0.25 to 1.24 nm^{-1} using parameterized amplitude and phase scattering waves calculated by FEFF 8 [26]. We note that XRD indicates that the 13 oxygen neighbors of Cs are dispersed in radial distances between 0.352 and 0.388 nm from the absorbing Cs. Similarly, the Cs–T radial distances range from 0.392 to 0.478 nm and the Cs–Cs radial distances range from 0.484 to 0.488 nm. Owing to the limited number of independent points in the spectrum [27], it is impossible to optimize all the parameters for all the neighbors. The number of fit parameters was reduced by grouping the Cs–O contributions in two average positions, the Cs–T contributions in one average position and the Cs–Cs contributions in two average positions. The best fit to the EXAFS, displayed in Fig. 5(a), is composed of five scattering paths. The agreement to the experimental data is quite good except at the ends of the transform range. The r-space comparison of the fit to the experimental data is shown in Fig. 5(b) and the quantitative fitting results are given in Table 3. For all scattering paths, the fitted number of atoms calculated is significantly lower than the crystallographic number of neighbors for the fitting region. This underestimation is the result of the simplification made by assigning average distances to the neighbors. Physically, the consequence of a large number of closely spaced neighbors is a destructive interference of the photoelectron contribution of each path. The resulting diminished EXAFS amplitude is not accurately represented by a single average amplitude. As a result, the number of atoms is not reported in Table 3 and only the average fitted distances are listed.

The fit to the EXAFS indicates that the Cs nearest neighboring oxygen atoms are distributed at two distances, 0.339 and 0.371 nm, and are in good agreement with the Cs–O distances reported for the tetrahedral pollucite structure by Palmer et al. [11]. In addition, the shorter Cs–O distance determined from the EXAFS analysis agrees well with the position of the third gaussian of PDF assigned to the T–T and Cs–O pairs.

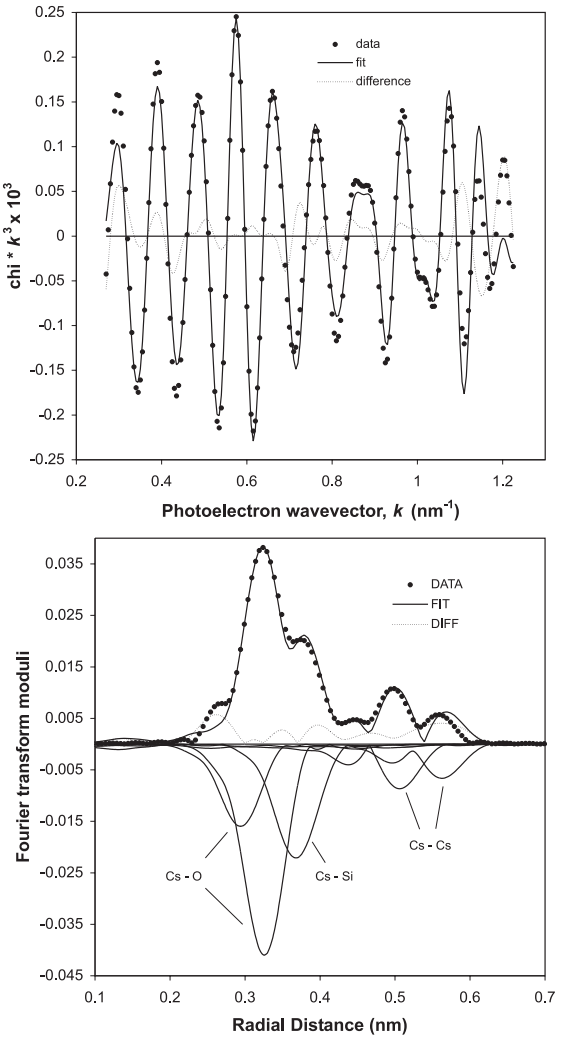

Fig. 5. (a) Fit to the filtered k^3-weighted EXAFS in wavevector-space. (b) Fourier transform moduli of all paths contributing to the total EXAFS in r-space.

The Cs–T distance at 0.413 nm, corresponding to the Si and Al atoms of the tetrahedra composing the six- and eight-membered rings, agrees well with the average Cs–T interatomic distance of 0.409 nm determined from the analysis of the diffraction data. The longer Cs–T distance at 0.456 nm, corresponding to one of the tetrahedra composing the four-membered rings that cap both ends of the eight-membered rings, was not detected in the EXAFS probably due to low photoelectron backscattering amplitude. Two distant Cs–Cs interatomic distances at 0.518 and 0.576 nm were observed in the fits to the EXAFS. The 0.518 nm Cs–Cs interatomic distance, corresponding to Cs atoms separated by the eight-membered rings, is approximately 0.035 nm longer than the distance determined by the analysis of the diffraction

Table 3
Metrical parameters from fit to EXAFS data for $CsAlSi_2O_6$ at 77 K

Scattering paths[a]	Metric parameters[b]	Cubic, Ref. [11]	Tetragonal, Ref. [11]	Experimental
Cs–O	d (nm)	0.337	0.324–0.352	0.339 ± 0.002
	n	6	6	n.d.[c]
Cs–O	d (nm)	0.352	0.360–0.390	0.371 ± 0.002
	n	6	7	n.d.
Cs–T	d (nm)	0.394, 0.413	0.392–0.415	0.4.13 ± 0.002
	n	6, 3	9	n.d.
Cs–T	d (nm)	0.452	0.426–0.478	0.476 ± 0.002
	n	6	6	n.d.
Cs–Cs	d (nm)	0.483	0.482	0.518 ± 0.002
	n	3	3	n.d.
Cs–Cs	d (nm)	0.591	0.578	0.576 ± 0.001
	n	2	2	n.d.
r^2				0.02648

[a] The scattering path is defined between the absorbing central atom, Cs, and each of the backscattering atoms. For all scattering paths $\delta E_0 = 8$ eV.
[b] d = interatomic distance, n = number of atoms.
[c] n.d. = not determined, see text for explanation.

data. On the other hand, the 0.576 nm Cs–Cs interatomic distance is in excellent agreement with the diffraction data. Attempts to adjust the EXAFS fit to shorter distances produced unrealistic parameters; a negative number of Cs atoms or exceedingly large delta E_0 values for this shell. Fits to the non-filtered EXAFS and EXAFS obtained by using a variety of splines also resulted in a 0.518 nm Cs–Cs interatomic distance for this shell, indicating that this longer distance is not likely an artifact of data processing.

4. Discussion

The interatomic distances determined by XRD, PDF, and EXAFS analyses are summarized and compared to the tetragonal structure of Palmer et al. [11] in Table 4. In general, the agreement is excellent and all techniques reflect the tetragonal character of the pollucite sample. The singular disagreement is the Cs–Cs distance determination along the [0 1 1] direction separating the eight-membered rings. The analysis of the XRD indicates that this distance is 0.485 nm while the EXAFS data indicates a substantially longer 0.518 nm distance. Both XRD and EXAFS techniques are more sensitive to Cs–Cs distance determinations because of the large number of electrons belonging to Cs relative to the other atoms in pollucite. While there is no obvious explanation for this disparity, the XRD determination will reflect the Cs–Cs separation that is averaged over a large number of unit cells, whereas the EXAFS determination will reflect only the local Cs–Cs separation. Perhaps the radiation-induced defects and presence of Ba^{2+} have increased the average Cs–Cs separation as seen by EXAFS but not in a correlated manner that would be detected by long-range, diffraction-based spectroscopy such as XRD. Fig. 6 summarizes the distortions of the pollucite structure determined by XRD relative to Palmer's tetragonal pollucite. In general, the aluminosilicate framework shows minor distortions that can be explained by small rotations along T–O–T bonds leading to increased puckering of the six- and eight-membered

Table 4
Interatomic distances in nm as determined by XRD, PDF, and EXAFS analyses

Interatomic distance	Ref. [11] at 298 K	XRD[a]	PDF	EXAFS
T–O	0.164	0.165	0.17	Not observed
O–O	0.269	0.267	0.25	Not observed
T–T	0.313	0.315	0.34	Not observed
Cs–O	0.335	0.335		0.339
		0.388		0.371
Cs–T	0.404	0.409	0.41	0.413
Cs–T	0.451	0.456	0.49	Not detected
Cs–Cs	0.482	0.485		0.518
Cs–Cs	0.578	0.576	0.57	0.576

[a] Reported number represents the average distance determined by analysis of XRD data.

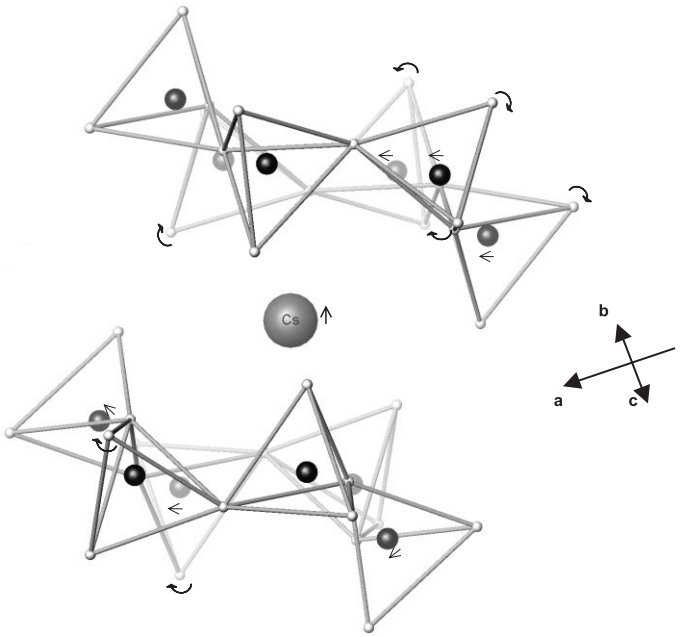

Fig. 6. Distortions of the tetragonal pollucite structure as determined from an analysis of the XRD data as seen looking in the [0 1 1] direction. The Cs atom is displaced along the [$\bar{1}$ 2 $\bar{2}$] direction toward the center of the upper six-membered ring. For clarity, only the edges of the TO_4 polyhedra are illustrated. Small rotations about the T–O–T angles that result in small displacements of the tetrahedral atoms, shown as small dark spheres, are indicated.

rings. In addition, the Cs atom is displaced along the [$\bar{1}$ 2 $\bar{2}$] direction towards the center of one of the six-membered rings. Thus, the beta radiation-induced effects lead to swelling of the lattice, as indicated by the slightly expanded lattice parameters for the tetragonal pollucite structure as well as puckering of the aluminosilicate channel encapsulating Cs.

Ewing et al. [28] and Weber et al. [5,6] provide extensive reviews of the current literature on radiation effects studies on ceramic and glass waste forms. However, there are only a few radiation effects studies on materials with an open aluminosilicate framework such as pollucite. Recent electron-beam irradiations on Na-aluminosilicates analcime, natrolite, and zeolite-NaY [29–31] provide compelling evidence of ionization-induced amorphization of this class of materials at relatively low absorbed doses. In addition, contrary to the behavior of the majority of crystalline aluminosilicates, the amorphization dose decreases with increasing temperature [29]. The results of these studies [29–31] suggest that self-irradiation from beta-decay may also result in the accumulation of defects that eventually lead to amorphization and that thermal self-annealing processes are not effective in retarding the accumulation of defects. The early stages of defect accumulation may manifest itself as small increases or decreases in lattice parameters and rotations about T–O–T bond angles as observed in this study.

Whether the accumulation of defects affects the mobility of Cs in pollucite and related open-framework aluminosilicates is critical for the assessment of long-term performance of waste forms. Only a few leaching studies following transmutation or irradiation of pollucite or closely related aluminosilicates have been done and seem to have contradictory results. In one of these studies [32], the transmutation of ^{137}Cs in pollucite has been simulated by the neutron radiation of ^{133}Cs-substituted pollucite. By this process, ^{133}Cs was converted to ^{134}Cs by neutron capture, which decays to Ba with a 2.06 years half-life and releasing a beta-particle with similar energy to the ^{137}Cs decay. Immediately following neutron irradiation, the pollucite sample was annealed at 1423 K for 1 h to remove the neutron damage effects and leach tests were conducted at one year intervals for two years. Although no appreciable change in density was observed, increases of 0.6% and 1.25% of Si and Cs were detected in the leachate after two years, respectively. The higher Si and Cs concentrations suggest that the transmutation of Cs to Ba results in decreased stability of the aluminosilicate framework and leads to enhanced mobility of Cs. A recent electron-beam irradiation study of Cs-substituted zeolite-NaY at about three orders of magnitude higher than the absorbed dose [31] suggests that the presence of Cs increases the resistance of the zeolite to radiation-induced amorphization and that the mobility

of Cs is decreased significantly on amorphization in subsequent leaching studies. The decreased mobility suggests that amorphization of the zeolite structure leads to the collapse of channels necessary for Cs migration. While the high beta doses necessary for amorphization will not be attained in Cs-bearing waste forms, the results of these two studies indicate that at low doses, prior to the onset of amorphization, the accumulated defects may lead to higher mobility and leachability of Cs; whereas once amorphization occurs, the Cs becomes trapped in the collapsed structure. Thus, the amorphous state, while unattainable by self-radiation from beta-decay, may be desirable for Cs retention. A more thorough analysis of the effect of accumulated defects from both transmutation and ionization processes on the pollucite structure is needed to assess the impact on Cs mobility.

5. Conclusions

XRD, PDF, and EXAFS analyses of beta irradiation of pollucite due to transmutation of $^{137}Cs^{+}$ to $^{135}Ba^{2+}$ indicates swelling of the pollucite lattice and suggest puckering of the aluminosilicate cage encapsulating Cs largely due to ionization processes. The effect of the lattice swelling and distortion of the local Cs environment is anticipated to increase the mobility of Cs at low damage levels. This behavior may impact the choice of waste form for the long-term disposal of ^{137}Cs, a fission product of uranium and a major contaminant at Department of Energy production facilities and necessitates detailed study of the accumulation of radiation defects in open framework materials.

Acknowledgements

The authors are very appreciative of Drs L.M Wang and B.X. Gu for sharing their results with us prior to publication which greatly assisted in the interpretation of our work. The authors also thank Dr D.T. Reed and S.B. Aase for their assistance in loading the pollucite samples and use of their facilities at Argonne National Laboratory, P.M. Villela and P. Franz for help in obtaining experimental data and useful discussions, and D. McCready for his help in XRD data analysis. Dr D.M. Strachan recognized the potential significance of these samples and obtained them from ORIS-CIS Bio International in 1991. XAFS and XRD experiments were performed at the Stanford Synchrotron Radiation Laboratory, which is operated by the US Department of Energy (DOE), Office of Basic Energy Sciences. This research was supported by the Environmental Management Science Program, Office of Science and Technology, Office of Environmental Management, DOE. However, any opinions, findings, conclusions, or recommendations expressed herein are those of the authors and do not necessarily reflect the views of DOE. The Pacific Northwest National Laboratory is operated by the Battelle Memorial Institute for DOE under contract DE-AC06-RLO 1830.

References

[1] J.L. Anchell, J.C. White, M.R. Thompson, A.C. Hess, J. Phys. Chem. 98 (1994) 4463.
[2] M.L. Balmer, Q. Huang, W. Wong-Ng, R.S. Roth, A. Santoro, J. Solid State Chem. 130 (1997) 97.
[3] Y. Su, M.L. Balmer, L. Wang, B.C. Bunker, N. Nyman, T. Nenoff, A. Navtrotsky, Mater. Res. Soc. Symp. Proc. 556 (1999) 77.
[4] G. Langlet, Nuclear Studies Center at Saclay, CIF-sur-Yvette, France, CEA-R-3853, 1969.
[5] W.J. Weber, R.C. Ewing, C.A. Angell, G.W. Arnold, A.N. Cormack, J.M. Delaye, D.L. Griscom, L.W. Hobbs, A. Navrotski, D.L. Prince, A.M. Stoneham, M.C. Weinberg, J. Mater. Res. 12 (1997) 1946.
[6] W.J. Weber, R.C. Ewing, C.R.A. Catlow, T. Diaz de la Rubia, L.W. Hobbs, C. Kinoshita, Hj. Matske, A.T. Motta, M.A. Nastasi, E.H.K. Salje, E.R. Vance, S.J. Zinkle, J. Mater. Res. 13 (1998) 1434.
[7] V.V. Murashov, J. Phys.: Condens. Matter 11 (1999) 1261.
[8] R.A. Young, in: R.A. Young (Ed.), The Rietveld Method, IUCR, Oxford University, New York, 1993.
[9] T. Egami, in: S.J.L. Billinge, M.F. Thorpe (Eds.), Local Structure from Diffraction, Plenum, New York, 1998.
[10] P.A. Lee, P.H. Citrin, P. Eisenberger, B.M. Kinkaid, Rev. Mod. Phys. 53 (1981) 769.
[11] D.C. Palmer, M.T. Dove, R.M. Ibberson, B.M. Powell, Am. Mineral. 82 (1997) 16.
[12] A.C. Larson, R.B. Von Dreele, Los Alamos National Laboratory, LA-UR-86-748, 1990.
[13] W.J. Dmowski, University of Pennsylvania, private communication.
[14] H.P. Klug, L.E. Alexander, X-Ray Diffraction Procedures for Policrystalline and Amorphus Materials, Wiley, New York, 1979, p. 795.
[15] K. Laaziri, S. Kycia, S. Roorda, M. Chicoine, J.L. Robertson, J. Wang, S.C. Moss, Phys. Rev. B 60 (1999) 13520.
[16] Th. Proffen, Michigan State University, private communication.
[17] I. Yanase, H. Kobayashi, Y. Shibasaki, T. Mitamura, J. Am. Ceram. Soc. 80 (1997) 2693.
[18] R.C. Ewing, W.J. Weber, F.W. Clinard Jr., Prog. Nucl. Energy 29 (1995) 63.
[19] Th. Proffen, S.J.L. Billinge, J. Appl. Cryst. 32 (1999) 572.
[20] A. Filipponi, A. Di Cicco, Phys. Rev. A 52 (1995) 1072.
[21] J.J. Rehr, C.H. Booth, F. Bridges, S.I. Zabinski, Phys. Rev. B 49 (1994) 12347.
[22] D.E. Ramaker, B.L. Mojet, D.C. Koningsberger, W.E. O'Grady, J. Phys.: Condens. Matter 10 (1998) 8753.

[23] H. Wende, P. Srivastava, R. Chauvistre, F. May, K. Baberschke, D. Arvanitis, J.J. Rehr, J. Phys.: Condens. Matter 9 (1997) L427.
[24] W.E. O'Grady, X. Quian, D.E. Ramaker, J. Phys.: Chem. B 101 (1997) 5624.
[25] D.E. Ramaker, X. Quian, W.E. O'Grady, Chem. Phys. Lett. 299 (1999) 221.
[26] A.L. Ankudinov, B. Ravel, J.J. Rehr, S.D. Conradson, Phys. Rev. B 58 (1998) 7565.
[27] S. Hasnain, X-Ray Absorption Fine Structure Spectroscopy VI, Ellis and Horwood, Chinchester, 1991.
[28] R.C. Ewing, W.J. Weber, W. Lutze, in: E.R. Merz, C.E. Walter (Eds.), Disposal of Weapon Plutonium, Kluwer, The Netherlands, 1996, p. 65.
[29] S.X. Wang, L.M. Wang, R.C. Ewing, J. Nucl. Mater., in press.
[30] E.C. Buck, Argonne National Laboratory, private communication.
[31] B.X. Gu, L.M. Wang, R.C. Ewing, J. Nucl. Mater. 278 (2000) 64.
[32] W.J. Gray, Nature 296 (1982) 547.